Investigating the Role of Gravity Waves on Mesosphere-Lower-Thermosphere (MLT) Inversion Layers at Low Latitudes (3-15^0)

Chalachew Lingerew[1*], U. Jaya Prakash Raju[1]

[1] Department of Physics, Washera Geospace, and Radar Science Laboratory, Bahir Dar University, Bahir Dar, Ethiopia

Correspondence to: Chalachew Lingerew (chalachewlingerew@gmail.com)

Abstract

The Mesosphere and Lower Thermosphere (MLT) transitional region, encompassing a height range of 60-100 km, is a distinct and highly turbulent zone within the Earth's atmosphere. This region is particularly significant due to dynamic processes like gravity waves, which contribute to the formation of the Mesospheric Inversion Layer (MIL). Investigating these phenomena is crucial for understanding the dynamics of the middle and upper atmosphere, especially regarding stability and energy transfer. Inversion layers significantly influence the stability of the atmosphere in this region, playing a crucial role in atmospheric dynamics. Inversion layers are associated with energy transfer processes, vital for understanding the overall dynamics of the atmosphere. Despite extensive study on an inversion, the formation mechanisms of mesospheric inversions remain poorly understood. This article explores the upper and lower inversion phenomena and their causative mechanisms. It uses long-term SABER observations from 2005 to 2020 over the latitude range of 3-15° N and longitude range of 33-48° E. The results show that the upper inversion occurs more frequently, with a frequency below 40%, compared to the lower inversion, which occurs below 20%. The upper inversion occurs within the height range of 78-91 km, with an inversion amplitude of approximately 20-80 K and a thickness of around 3-12 km. In contrast, the lower inversion is confined to the height range of 70-80 km, with an inversion amplitude of about 10-60 K and a thickness of around 4-10 km. Moreover, the gravity wave indicator potential energy shows high energy (below 100 J/kg) in the upper mesosphere region (85-90 km) compared to the lower mesosphere region (70-75 km) with less than 50 J/kg. Considering gravity waves, the Brunt-Väisälä frequency (N^2) stability criteria indicate instability in the upper mesosphere region with very low values compared to the lower mesosphere region. This suggests that the high amount of gravity wave potential energy is a consequence of the higher instability in the upper inversion compared to the lower inversion.

Keywords: Mesosphere and Lower Thermosphere (MLT), Upper and Lower Inversions, Perturbed Temperature, Causative Gravity Waves, Potential Energy, Brunt-Väisälä Frequency, Atmospheric Instability.

Introduction

The Mesosphere and Lower Thermosphere (MLT) region serves as a transitional zone for wave processes from the lower and upper atmospheres, including tidal, planetary, and gravity waves. Gravity waves (GWs) originating from the lower atmosphere are known to propagate into the mesosphere. There, they break and dissipate their energy and momentum, affecting the thermal structure, global atmospheric circulation, and variability of the mesosphere. This process also influences the formation of mesospheric inversion layers (MILs), which are associated with increased temperature variability in the mesosphere. MILs indicate wave saturation when the lapse rate falls below the dry adiabatic lapse rate (Sica et al., 2007). Temperature inversions in the mesosphere have been widely observed and studied using various techniques, including lidar, radar, rocket sondes, and satellites, across different geographic locations. Sivakandan et al. (2014) utilized TIMED/SABER kinetic temperature data to examine the occurrence and characteristics of mesospheric inversions over the equatorial Indian region (0 to 10° N and 70 to 90° E) for the years 2002 and 2008. However, they did not explore the causative factors. This study aims to investigate the causes of these inversions, focusing specifically on the role of atmospheric gravity waves.

Gravity waves and mesospheric inversion layers (MILs) are interconnected phenomena within the Earth's atmosphere, particularly in the mesosphere and lower thermosphere. MILs are layers within the mesosphere where the temperature profile shows an inversion. This means the temperature increases with altitude, contrary to the typical decrease. These inversion layers often form due to dynamic processes, including the breaking and dissipation of gravity waves. As gravity waves propagate upwards, they can grow in amplitude because the atmospheric density decreases with altitude. When these waves reach a critical amplitude, they become unstable and break. This breaking process releases energy and momentum into the surrounding air, causing localized heating. The energy dissipation from breaking gravity waves causes localized heating. This heating can create or enhance mesospheric inversion layers by increasing the temperature at certain altitudes. The breaking of gravity waves can also generate turbulence, which further influences the structure and stability of inversion layers. This process also contributes to momentum and energy deposition.

The momentum and energy deposition of gravity waves (GWs) are believed to be key drivers of large-scale atmospheric circulation, the coupling of different atmospheric layers, and inversion phenomena (Fritts and Alexander, 2003; Lindzen, 1981; Smith, 2012). Additionally, researchers are exploring the influence of gravity wave-breaking on mesosphere dynamics to understand its

impact on inversion phenomena, particularly in mid- and high-latitude regions (Gan et al., 2012; Walterscheid and Hickey, 2009; Collins et al., 2011; Szewczyk et al., 2013). Both observational and modeling studies have investigated GWs as a cause of these inversions (Fritts, 2018; Collins et al., 2014; Sridharan et al., 2008; Ramesh and Sridharan, 2012; Ramesh et al., 2013, 2014, 2017). Despite extensive exploration, our understanding of the impact of gravity waves on mesosphere inversions, particularly in terms of temperature variability, remains incomplete, especially in mid- and high-latitude regions (Singh and Pallamraju, 2018; Fritts et al., 2018). As a result, the study of inversion phenomena and their underlying causes remains a key area of focus in mesosphere dynamics research.

Research on the temporal and spatial variability of the mesosphere inversion phenomenon, particularly about atmospheric waves and gravity wave activity, is notably lacking in low latitudes. To address this gap, our study investigates the mesosphere inversion phenomenon and its association with gravity wave activity and stability criteria. We use Brunt-Vaisala frequency (N^2) over the low latitudinal band (3°–15° N) with long-term SABER observations from 2005 to 2020. The study is organized as follows: Section 2 details the data and methodology used to analyze the mesosphere inversion phenomenon and their causative gravity waves via the potential energy. Section 3 presents the results, and Section 4 concludes the findings.

2. Observation and Data analysis

2.1 SABER Observation

The TIMED/SABER satellite, launched on December 7, 2001, operates in an elliptical orbit at approximately 625 km altitude with a 74° inclination relative to the equator. Since its launch, SABER has been a crucial tool for atmospheric research, providing extensive data on the middle atmosphere. SABER is a limb-viewing radiometer working in the infrared region (1.27–17 microns) and can measure radiative emissions across a wide range of altitudes. It offers nearly global coverage and continuous 24-hour data over 60 days. The instrument completes 15 orbits daily, each taking about 97 minutes, and collects around 1400 data profiles per day, with each profile taking 58 seconds. SABER's high-resolution temperature profiles are essential for studying the dynamics and wave processes in the mesosphere. It provides temperature measurements with an accuracy of 1 to 2 K between 15 and 60 km. The accuracy decreases to 5 K below 85 km and increases to 6.7 K to 10 K near 100 km. This data has been instrumental in understanding the thermal structure and dynamical processes in the mesospheric region, as highlighted by various studies (Garcia et al., 2008; Gan et al., 2012, 2014; Bizuneh et al., 2022; Lingerew et al., 2023;

98 Rezac et al., 2015; Meriwether and Gerrard, 2004; Fechine et al., 2008; Dou et al., 2009; France

99 et al., 2015).

100 We utilized SABER vertical temperature profiles taken within the 60–100 km altitude range. These

101 profiles cover the period from 2005 to 2020, spanning latitudes from 3°N to 15°N and longitudes

102 from 33°E to 48°E. Figure 1 shows the monthly mean of SABER temperature data for the

103 mesosphere and lower thermosphere. The data aim to illustrate the MLT temperature variability,

104 which helps us identify the inversion layers (MIL). The monthly mean temperatures in the MLT

105 region show a maximum of 200-240 K at altitudes of 60-70 km. Then it decreases to around 160-

106 180 K at 95-100 km throughout the entire period. While the temperature patterns in the 70-90 km

107 altitude range suggest an inversion, these inversions are not visible.
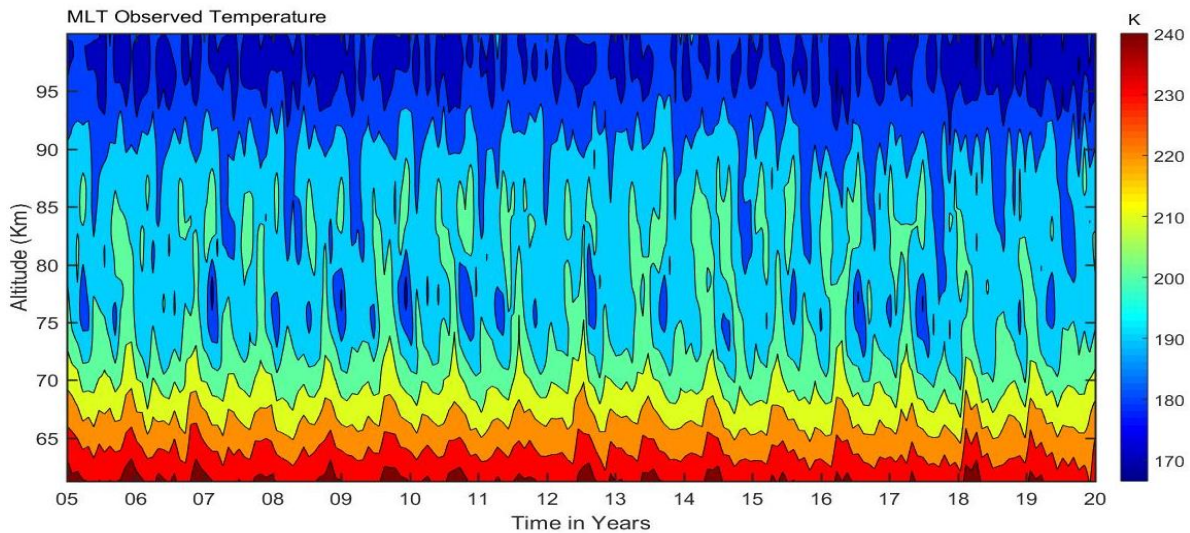
108
109 **Figure** 1. The monthly mean of MLT temperature variability in the height range of 60-100 km

110 during 2005-2020 over the low-latitude.

111 **2.2 Analysis Technique**

112 The Earth's middle atmosphere typically has a negative temperature gradient, but some reports

113 have shown positive temperature gradients in the mesosphere (Meriwether and Gardner, 2000;

114 Gan et al., 2012). This phenomenon is called the "mesospheric inversion layer (MIL)". MILs are

115 identified using a procedure detailed by Leblanc and Hauchecorne (1997) and Fechine et al.(2008).

116 Mesospheric inversions are characterized by their thickness (the altitude difference between

117 maximum warming and cooling) and amplitude (the temperature difference between these points)

118 (Meriwether and Gardner, 2000). Here are the identification criteria for these inversions:

119   1. The bottom level of the lower inversion is above 70 km, and the top level is below 80 km.

120   For the upper inversion, the bottom level is above 80 km, and the top level is below 92 km.

121   2. The amplitude is considered larger than 5 K.

122   3. The thickness is greater than or equal to 3 km.
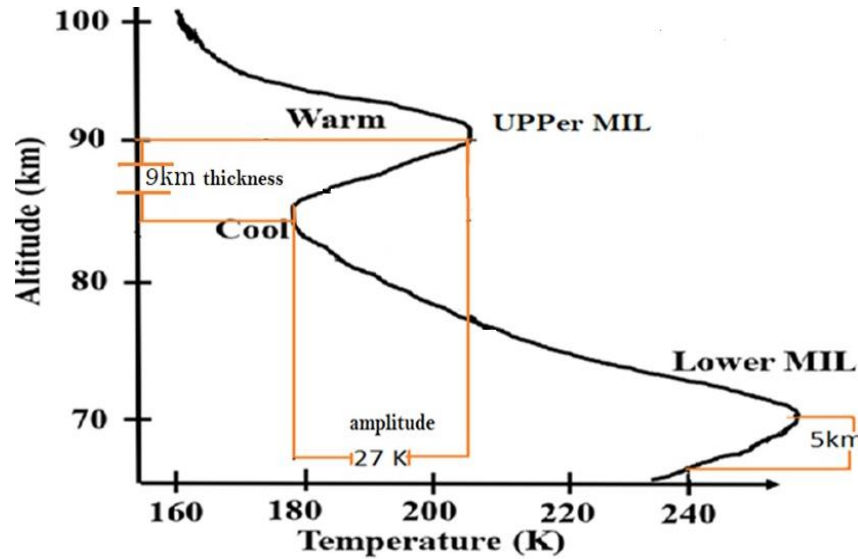
123

124 Figure 2. Schematic of upper and lower mesospheric inversion layers shown in the temperature

125 profile for the MLT regions (Adapted from Meriwether and Gerrard, 2004).

126 Figure 2 illustrates this concept, showing a positive temperature difference between the top and

127 bottom levels of the inversion. This method has been utilized in numerous previous studies

128 investigating mesospheric inversions (Leblanc et al., 1998; Meriwether and Gardner, 2000; Duck

129 et al., 2001; Duck and Greene, 2004; Cutler et al., 2001; Siva Kumar et al., 2001; Ratnam et al.,

130 2003; Gan et al., 2012). The frequency occurrence rate of mesospheric inversion layers (MILs) is

131 derived during the period 2005–2020 in the upper and lower MLT regions. This rate is calculated

132 by dividing the number of inversion days in each month by the total number of days in that month

133 over the 16-year observation period (2005–2020).

134 Mesospheric temperature inversions are related to instabilities in atmospheric dynamics. To

135 identify the causative, short-period atmospheric gravity waves, a high-pass filter with a one-hour

136 interval cutoff frequency is applied using the Brunt-Väisälä frequency (N2). Another important

137 concept to estimate the Brunt-Vaisala frequency is the potential temperature (θ). It represents the

138 air parcel's temperature when it is displaced adiabatically to a standard pressure level, p_0, from the

139 current pressure level, p. This is based on the first law of thermodynamics.

140
$$\frac{dT}{T} = \frac{R}{c_p}\frac{dp}{p} \Rightarrow \int_T^0 \frac{dT}{T} = \int_p^{p_0} \frac{R}{c_p}\frac{dp}{p}$$
(1) it yields

141
$$\theta = T\left(\frac{p_0}{p}\right)^{R/c_p}$$
(2)

142 Therefore, the motion of a vertical atmospheric air parcel can be described by (Liu, 2011; Vadas

143 and Fritts, 2005) as follows in equation (2.3). This equation calculates the Brunt-Vaisala frequency

144 of the parcel due to the buoyant and gravitational forces acting on it.

145
$$\frac{d^2 s}{dt^2} = -g\frac{\rho - \rho_0}{\rho}\ sina$$
(3)

146 Based on the hydrostatic equation, $\rho = \rho_0$, and $p = p_0 \Rightarrow \frac{\partial p}{\partial z} = \frac{\partial p_0}{\partial z} = -g\rho_0$ (4) and the ideal gas

147 law, $\rho = p/RT = p_0/RT$ gives the parcels motion of an equation:

148
$$\frac{d^2 s}{dt^2} = -\frac{g}{\rho}\left(\frac{d\rho}{dp}\frac{\partial p_0}{\partial z} - \frac{\partial \rho_0}{\partial z}\right)z$$
(5)

149 Following the same approach using the hydrostatic equation (4) and adiabatic equation (6)

150
$$dln\rho = \frac{dlnp}{\gamma}, \gamma = c_p/c_v$$
(6) yields

151

152
$$\frac{d^2 s}{dt^2} = -\frac{g}{\rho}\left(\frac{\rho}{\gamma p_0}\frac{\partial p_0}{\partial z} - \frac{\partial \rho_0}{\partial z}\right)z = g\left(\frac{\partial ln\rho_0}{\partial z} - \frac{1}{\gamma}\frac{\partial lnp_0}{\partial z}\right)z$$
(7)

153 For the ideal gas law of p = ρRT, the natural logarithm is taken for altitude, z on both sides, yielding

154
$$\frac{\partial ln\rho}{\partial z} = \frac{\partial lnp}{\partial z} - \frac{\partial lnT}{\partial z}$$
(8)

155 Then after, the potential temperature (θ) of the parcel is calculated as follows based on the equation

156 (2):

157
$$\frac{\partial ln\theta}{\partial z} = \frac{\partial lnT}{\partial z} - \frac{R}{c_p}\frac{\partial lnp}{\partial z} = \frac{1}{T}\left(\frac{\partial T}{\partial z} + \frac{g}{c_p}\right) = \left(1 - \frac{R}{c_p}\right)\frac{\partial lnp}{\partial z} - \frac{\partial ln\rho}{\partial z}$$
(9) to derive the Parcels

158 acceleration based on equations (7) to become:

159
$$\frac{d^2 s}{dt^2} = -g\frac{\partial ln\theta_0}{\partial z}z\ sina = -g\frac{\partial ln\theta_0}{\partial z}ds.sin^2 a$$
(10)

160 Whereas by introducing the frequency, N, with $N^2 = g\frac{\partial ln\theta_0}{\partial z}$

161 The Brunt-Vaisala frequency, N^2 is calculated based on the following mathematical formulation

162 used to characterize atmospheric stability.

163
$$N^2(z) = \frac{g(z)}{T_0(z)}\left(\frac{\partial T_0(z)}{\partial z} + \Gamma_d\right)$$
(11)

164 Where g is the acceleration due to gravity, N is the Vaisala frequency, T_0 is the background

165 temperature (estimated based on third-order polynomial fitting), $\Gamma_d = g/c_p$ is the adiabatic lapse

166   rate, and $c_p = 1004\,J\,K^{-1}\,kg^{-1}$ is the specific heat capacity of the atmosphere at constant

167   pressure. When the Vaisala frequency, N^2, is positive, the atmosphere is stable. When N^2 is

168   negative, the atmosphere is unstable. In this case, the atmospheric lapse rate, $\Gamma = -\frac{\partial T}{\partial z}$, is larger

169   than the adiabatic lapse rate, $\frac{g}{c_p} \approx 9.5\,K\,km^{-1}$. To estimate the Brunt-Vaisala frequency, a

170   third-order polynomial fit of the least squares has been applied to the SABER observed

171   temperature (T) profile to estimate the background temperature (T0), following the procedure of

172   Leblanc and Hauchecorne (1997). After estimating the perturbed temperature (Tp) from equation

173   (12), it is identified by subtracting the background temperature from the observed temperature data

174   (T).

175
$$T_p = T - T_0 \qquad\qquad (12)$$

176   After estimating the perturbed temperature (Tp), a high-pass band filter is applied. This filter

177   removes low-frequency components associated with planetary and tidal waves, retaining the high-

178   frequency components related to short-period gravity waves (John and Kumar, 2012). This process

179   isolates the influence of gravity waves and accurately calculates their potential energy. The high-

180   pass filter is based on known frequency ranges, typically below the periods of short-period gravity

181   waves (e.g., <1 hour).

182
$$E_p(z) = \frac{1}{2}\left(\frac{g(z)}{N(z)}\right)^2 \left(\frac{T_p{'}(z)}{T_0(z)}\right)^2 \qquad\qquad (13)$$

183   The potential energy of the waves, a function of altitude (z), is used to determine the impact of

184   atmospheric gravity waves on atmospheric inversions.

185   **3. Results and discussion**

186   **3.1 Identification and Characteristics of the Lower and Upper MLT Inversion**

187   Daily SABER temperature profiles, covering altitudes of 60–100 km from 2005 to 2020, are shown

188   in the contour plots of Figure 3. Figures 3 (a and b) depict the upper mesosphere, while Figures 3

189   (c and d) show the lower mesosphere. The horizontal panels of Figures 3 (a) and 3 (c) show

190   observed temperatures ranging from approximately 180–220 K, before accounting for inversion

191   layers. The horizontal panels of Figures 3 (b) and 3 (d) show inversion day temperatures, ranging

192   from 180–225 K. These inversion day temperatures are higher than those shown in Figures 3 (a)

193   and 3 (c). This indicates that maximum temperatures occur on inversion days in both the upper

194   and lower MLT regions.
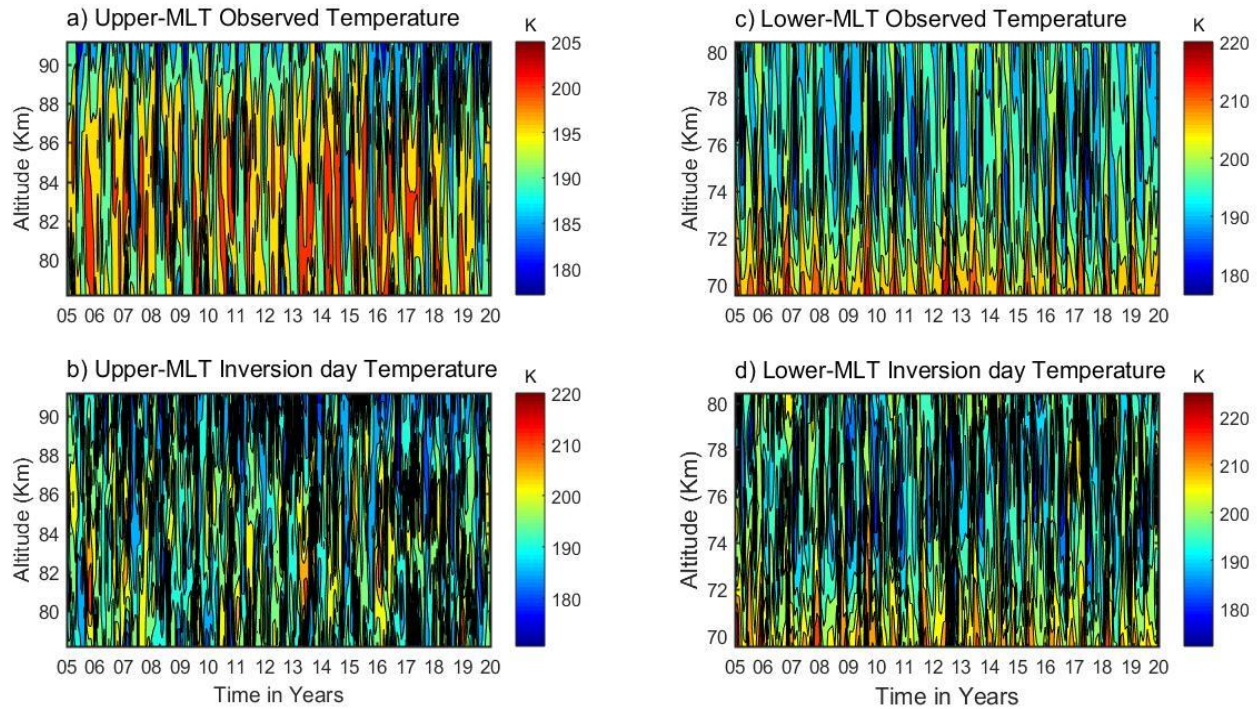
Figure 3. The upper and lower mesosphere observed temperatures in the first horizontal panel at (a and c) with their inversions in the second horizontal panel at (b and d).

The upper left panel of Figure 3(a) shows the observed temperature in the upper mesosphere. It ranges from approximately 180–205 K at altitudes of around 80–90 km. The upper right panel of Figure 3(c) shows the lower mesosphere, with temperatures ranging from about 180–220 K at altitudes of approximately 70–80 km. In contrast, the lower left panel of Figure 3(b) shows an upper-mesosphere inversion day temperature. It ranges from 180–220 K at an altitude of approximately 80–90 km. The lower right panel of Figure 3(d) shows a lower-mesosphere inversion day temperature. It ranges from 180–225 K at an altitude of approximately 70–80 km. These inversion day temperatures in Figures 3(b) and 3(d) suggest a temperature gradient shifting from negative to positive. This could be due to factors such as atmospheric gravity waves, chemical reactions, or solar radiation. Our temperature observations for the lower MLT region on an inversion day, within the altitudinal range of 70–80 km, align with those reported by Sivakumar et al. (2001). They identified inversion day temperature variability in the altitudinal range of 73–79 km. Additionally, Sivakandan et al. (2014) examined mesospheric inversions in the 60–105 km altitude range over low-latitude regions. Their findings closely match our results.
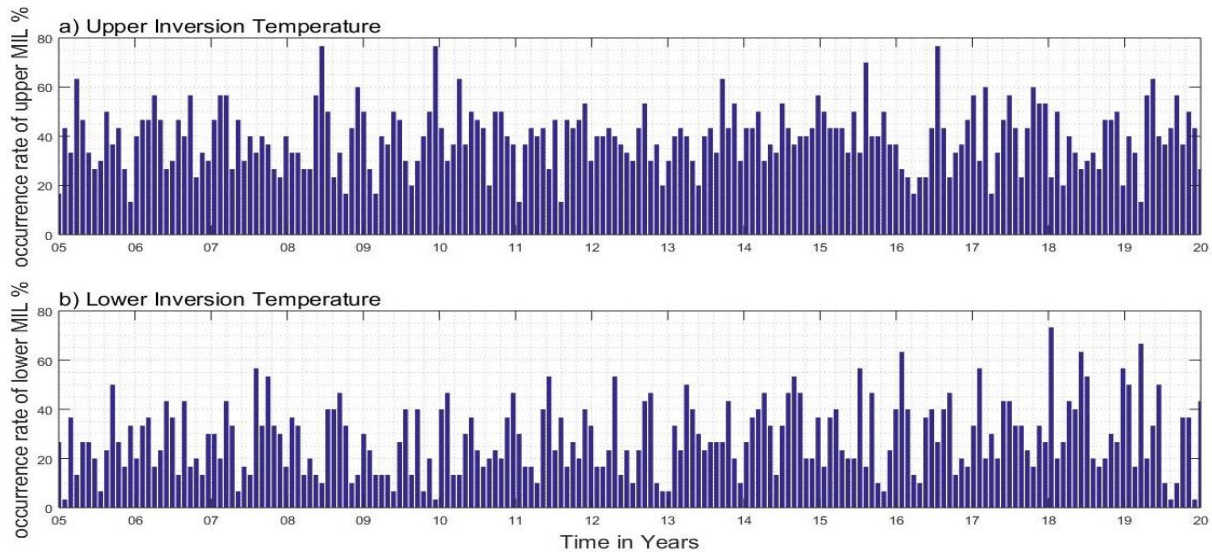
Figure 4. The frequency occurrence rate (percentage) of the (a) upper and (b) lower inversion temperatures during 2005-2020 over low latitudes.

Figure 4 shows the frequency occurrence rate (%) of mesospheric inversion layers (MILs) in histograms. Figure 4(a) shows the occurrence rate for upper MILs, while Figure 4(b) shows the rate for lower MILs. The mean frequency occurrence rate of upper inversions is approximately below 40%. Peak rates range from 60% to 78%, notably in the years 2008, 2010, and mid-2016. In contrast, the mean occurrence rate for lower inversions is below 20%. Overall, the occurrence rate for upper inversions is relatively higher compared to lower inversions. This may be related to atmospheric wave activities, mainly gravity waves. Hauchecorne et al. (1987) and France et al. (2015) discuss the effects of gravity waves on inversion variability in the upper and lower mesosphere. Based on these findings, Figure 5 examines the characteristics of inversion layers, including their amplitude and thickness. Figure 5 illustrates the characteristics of mesospheric temperature variability on an inversion day. It focuses on base height, amplitude, and thickness, before examining the effects of gravity waves on an inversion. Histograms show the frequency of amplitude, thickness, and base height for inversion day MLT temperature variability. These histograms feature best-fit Gaussian distribution curves, represented by red lines. The observed distributions align with Gaussian curves, indicating that the number of mesospheric inversion layers (MILs) follows a normal distribution. This suggests that the attributes are real-valued random variables. The left column has three rows showing histograms of (a) amplitude, (b) thickness, and (c) base height of the inversion day temperature variability for the upper MLT. These histograms also include their statistical values, mean, and standard deviations (SD). The corresponding right column has three rows representing (d) amplitude, (e) thickness, and (f) base height of the inversion day temperature variability for the lower MLT region.
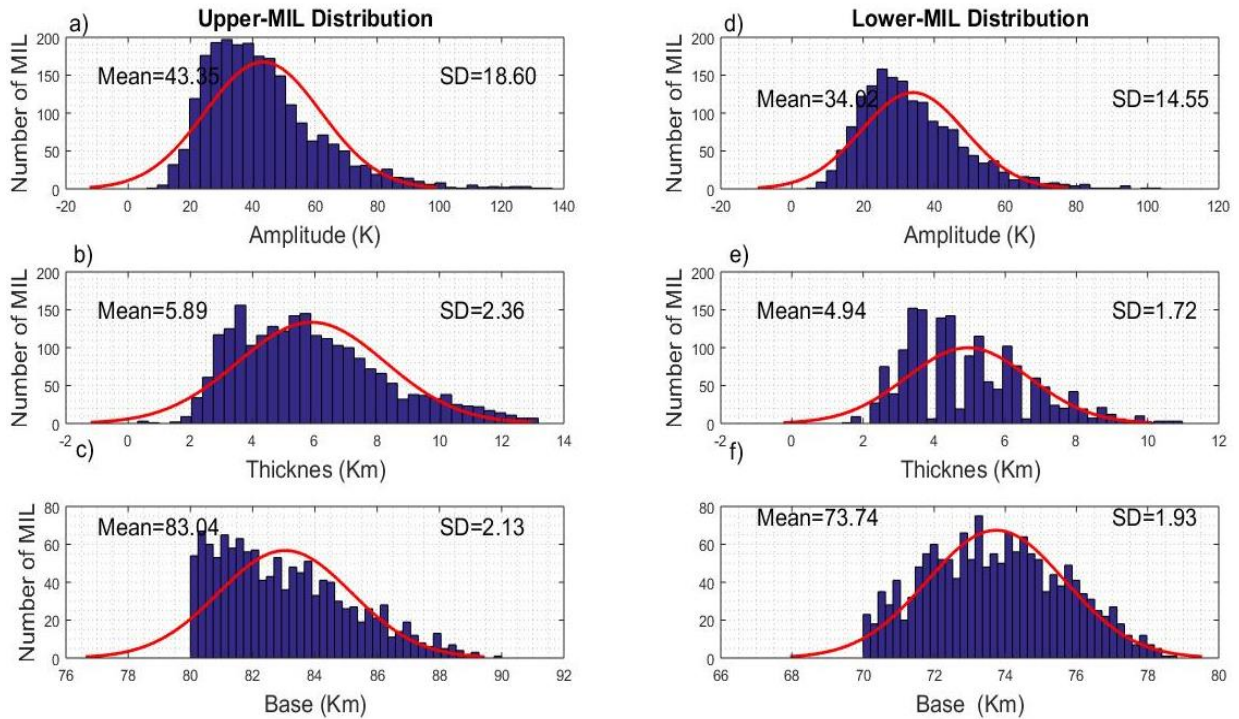
Figure 5. The histograms depict the occurrence of MLT inversion day temperature variability. The first vertical panel shows the distribution of (a) amplitude, (b) thickness, and (c) base height for the upper inversion day. The second vertical panel presents the corresponding distribution for the lower inversion, including (d) amplitude, (e) thickness, and (f) base height.

The amplitude of upper inversion day temperature variability in Figure 5(a) ranges between 20 and 80 K, with a peak value of 38 K. This follows a Gaussian distribution with a large standard deviation (SD) of 18.6. The thickness of the inversion layer for upper MILs, shown in Figure 5(b), ranges from 3 to 9 K. The most probable value is 5.5 K, with a low SD of 2.3. The base height of the upper MIL in Figure 5(c) spans from ~80 to 90 km, with a peak value of around 83 km. This indicates a large number of upper MLT inversions, with an SD of 2.13. The highest number of upper inversions between 2005 and 2020 is observed at 82 km. This may be attributed to gravity wave breaking and energy dissipation, influenced by waves generated from lower atmospheric regions and solar flux impacts. The lower inversion amplitude, depicted in Figure 5(d), ranges between 10 and 60 K, with a peak value of 25 K and a standard deviation (SD) of 14.5. The thickness of the lower inversion, shown in Figure 5(e), ranges from 3 to 8 km, with the most probable value at 3.8 km and a low SD of 1.72. The base height of the lower inversion in Figure 5(f) ranges from 70 to 80 km, with a peak value of around 74 km and a lower SD of 1.93. Previous investigations by Sivakandan et al. (2014) from the Indian sector reported amplitudes ranging from 14–39 K in 2002 and 15–42 K in 2008. The thicknesses ranged between 2.7–7.5 km in 2002 and

256 2.8–7.3 km in 2008, under the influence of solar flux. These findings align well with the present
257 study, indicating no significant variation in characterizing mesospheric inversion based on
258 amplitude and thickness in the low-latitude region within the altitude range of 60 to 90 km.

3.2   Latitudinal Variations of Mesospheric Inversion Layers (MILs)

260 This section examines the spatiotemporal (latitudinal-time) variability of upper and lower
261 mesosphere inversion phenomena. Contour plots of time vs. latitude in Figures 6 and 7,
262 respectively, characterize this variability based on amplitude, thickness, and base height over the
263 low-latitude band (3-15°) during 2005–2020. The Upper MILs phenomenon is observed around
264 80–90 km. The maximum amplitude, in the range of 90–120 K, occurs over latitude bands (5-12°)
265 during 2005, 2007, mid-2011, 2013, 2015, 2016, mid-2019, and 2020 (Figure 6(a)). The second
266 horizontal panel in Figure 6(b) shows the inversion thickness, with a maximum range of ~(8–12
267 km) across the entire latitudinal region (3-15° N). Figure 6(c) shows the relative maximum
268 inversion base height, around ~(84-88 km), in the latitudinal range between 4° and 14° N during
269 2006, 2008, 2010, 2012, 2016, and 2018.
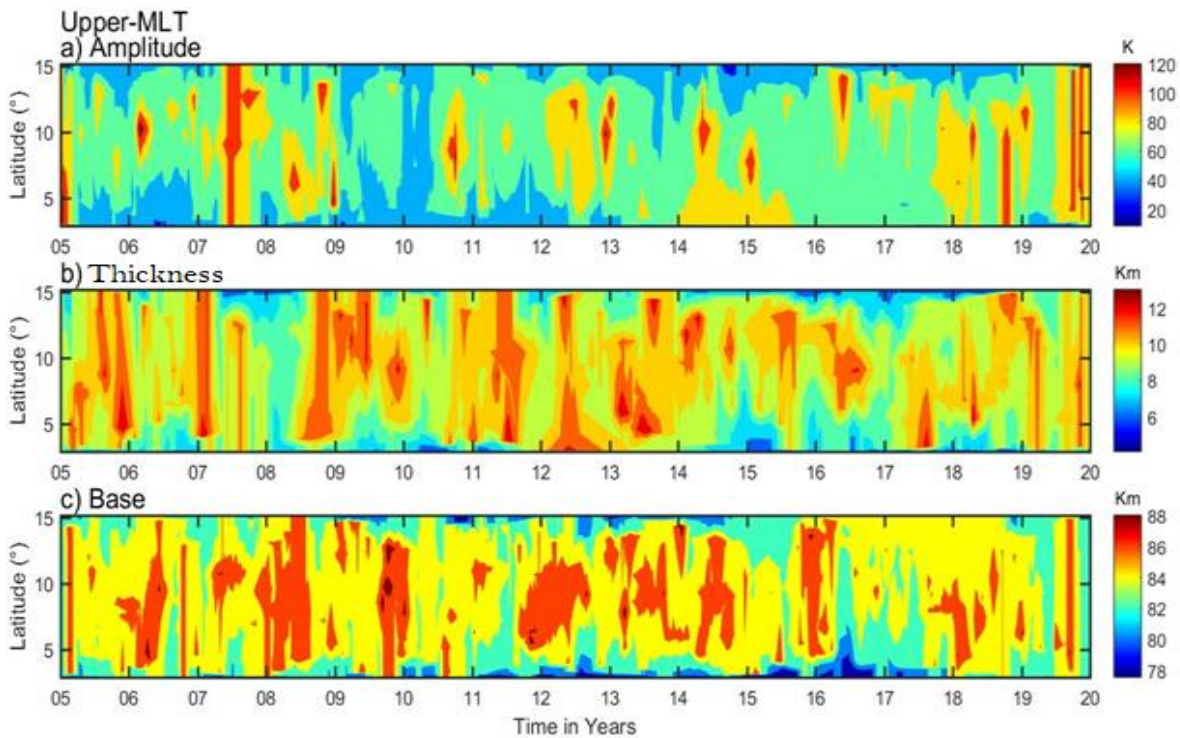
270
271 **Figure** 6. The daily upper inversions (~80-90 km) of (a) amplitude, (b) thickness, and (c) base
272 height during 2005-2020 over latitudinal variation.
273 Contour plots in Figure 7(a, b, and c) show the latitudinal variations of the lower inversion (MILs)
274 phenomenon, based on amplitude, thickness, and base height, respectively. These plots cover an
275 altitudinal range of ~70-80 km. The lower inversion amplitude generally ranges from ~30-60 k

276 across all latitudinal bands. However, it reaches a maximum range of ~(80-100 k) during 2013,

277 2015, 2016, and 2019 in various latitudinal regions between 5 and 140 N. Figure 7(b) shows an

278 inversion thickness of 5-7 km across the entire latitude band, except for a maximum thickness of

279 8-10 km. Figure 7(c) shows a base height of 76-80 km for most latitudes and periods. However,

280 there are exceptions: 2008, 2014, and mid-year 2018 exhibit a maximum base height.
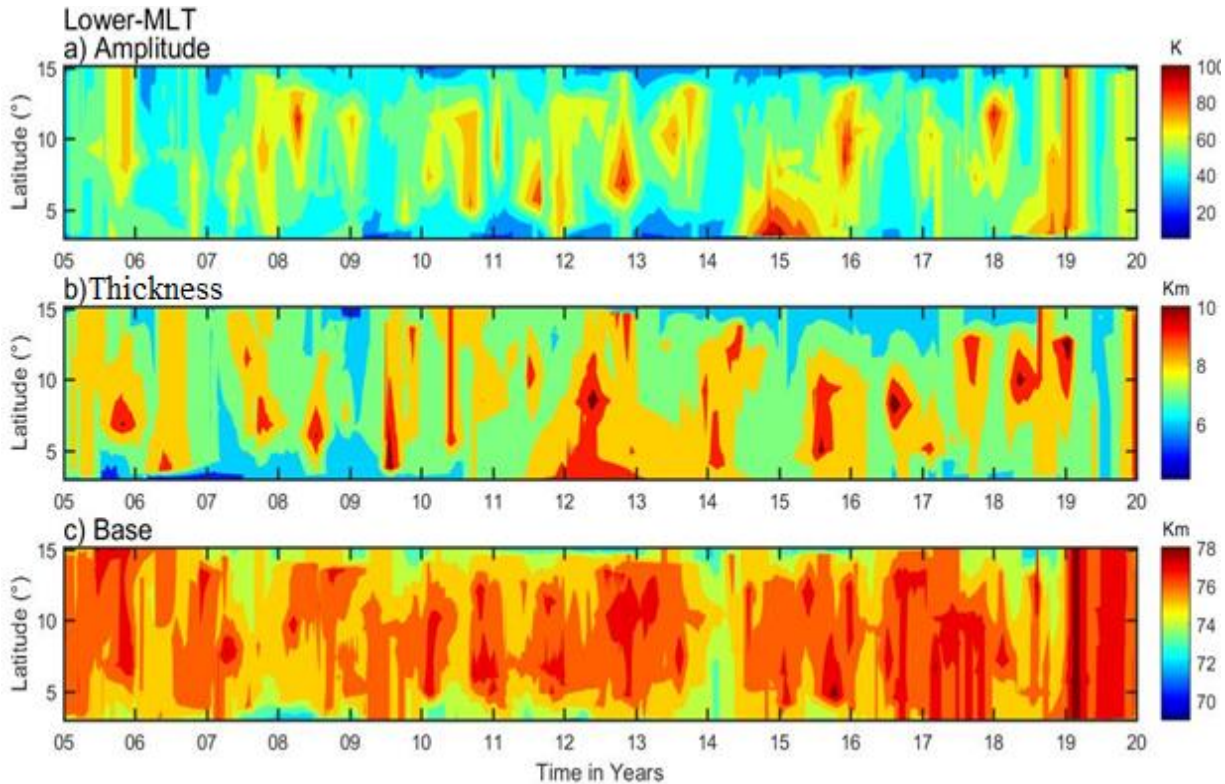
281

282 **Figure** 7. Same as Figure 5, but for the lower mesosphere inversions (~70- 80 km).

283 Figures 6 and 7 demonstrate that the upper inversion exhibits higher amplitude and thickness

284 compared to the lower inversion, suggesting a highly dynamic phenomenon in the upper

285 mesosphere region. Satellite measurements, particularly those from TIMED/SABER, provide

286 valuable insights into latitudinal variations in MILs. These observations confirm that MILs also

287 occur at low latitudes (Gan et al., 2012).

288 ### 3.3   Separations of the Perturbed Temperature in the Mesosphere Region

289 The perturbed temperature (T_P) of the upper and lower MLT inversions during the period of 2005-

290 2020 can further be used to calculate their derived potential energy of gravity waves and the Brunt-

291 Väisälä frequencies (N^2). First, the upper-temperature inversion profiles are identified in the MLT

292 region during the entire observational period of 2005-2020, as displayed in the contour plot of

293 Figure 8(a). The observed temperature ranges from ~170-220 K with minimal variability. A 3rd-

294 order polynomial fit is applied to calculate the background temperature (T_0), as shown in the

295   contour plot of Figure 8(b). This background temperature exhibits periodic variability over an

296   altitude of around ~82-87 km, ranging from ~195-197 K. The perturbed temperature profiles (Tp),

297   calculated as the difference between the observed inversion temperature (T) and the corresponding

298   background temperature profiles (T$_o$), range from -25 to +25 K, as shown in Figure 8(c).

299
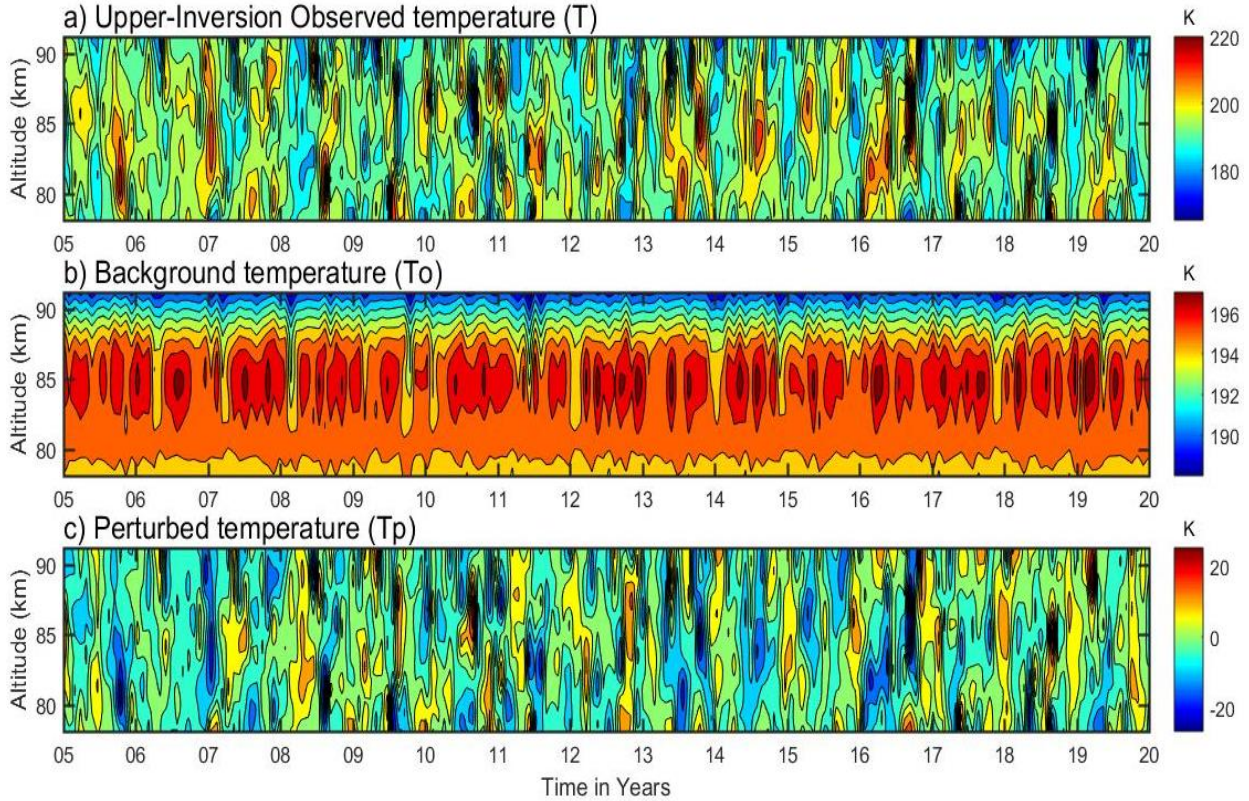
300   **Figure** 8. The upper mesosphere temperatures in the vertical panel are: (a) inversion day observed

301   temperature; (b) background temperature; and (c) perturbed temperature in the upper mesosphere

302   region.

303   A similar procedure is used to calculate the perturbed temperature (T$_P$), observed temperature, and

304   background temperature in the lower mesosphere region from 2005 to 2020. Their corresponding

305   contours are displayed in Figure 9(a-c). In Figure 9(a), the observed temperature of the lower

306   inversion ranges from ~170-220 K. The background temperature of the lower inversion ranges

307   from ~ 195-210 K, with maximum values of ~200-210 K at a height of ~70-72 Km, as shown in

308   Figure 9(b). The perturbed temperature in Figure 9(c) ranges from -25 to 20 K. Notably, the upper

309   mesosphere perturbed temperature is at its maximum compared to the lower mesosphere region,

310   possibly due to a highly dynamic phenomenon.
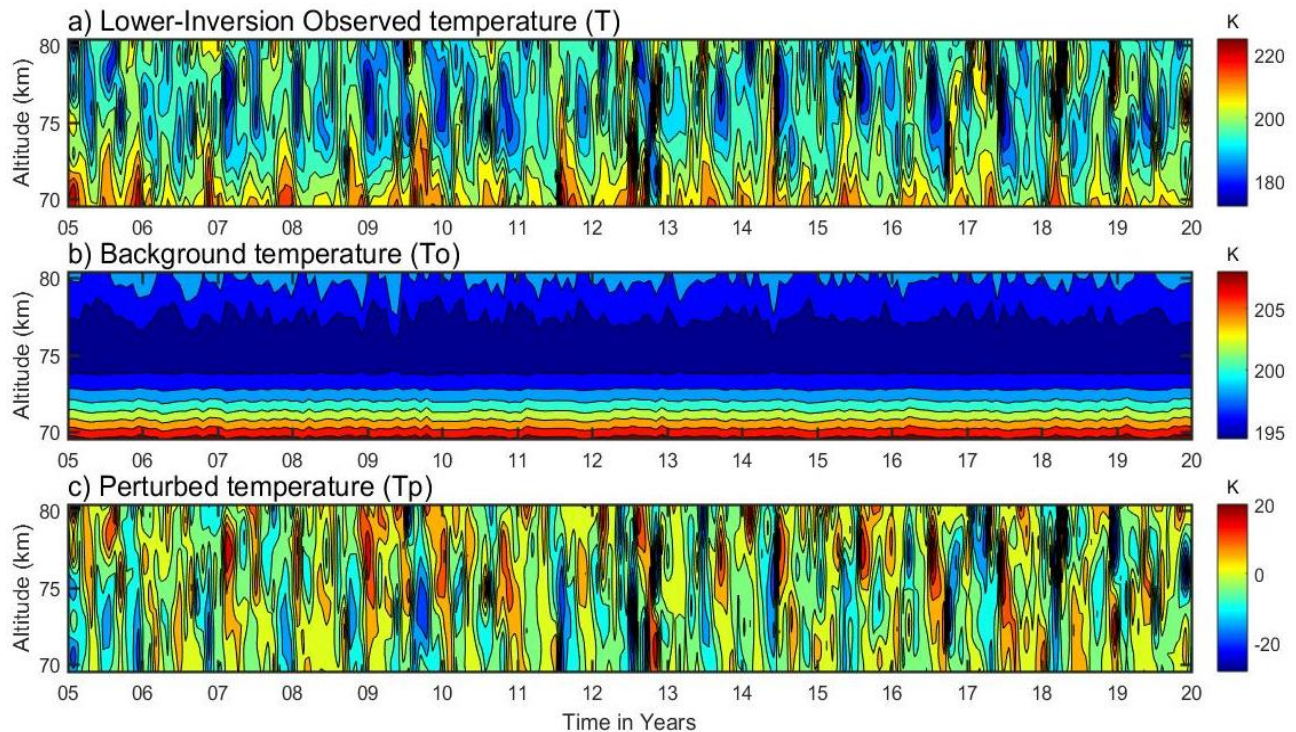
Figure 9. Same as Figure 7, but for the lower mesosphere atmospheric region.

3.4 Effects of Gravity Waves on Mesosphere Inversions and Associated Instability

Gravity waves occur when air parcels oscillate due to the restoring force of gravity after being displaced vertically. These waves are generated by various processes, including airflow over mountains, convection, and wind shear. Gravity waves and mesospheric inversion layers (MILs) are interconnected phenomena, particularly in the mesosphere. MILs are layers within the mesosphere where the temperature profile shows an inversion, meaning the temperature increases with altitude, unlike the typical decrease. These inversion layers often form due to dynamic processes, such as the breaking and dissipation of gravity waves. When vertically propagating waves break and dissipate, they transfer their energy and momentum into the atmosphere. This significantly affects the thermal structure, particularly increasing mesospheric temperature variability with elevation, a phenomenon known as the inversion (see Figure 11). Studies by Holton et al. (2003) and Holton and Hakim (2013) have demonstrated the connection between the potential energy of gravity waves and inversions.

This section explores the longitudinal variability of gravity waves' contribution to mesospheric inversion layers (MILs). The investigation involves calculating potential energy and assessing instability using the Brunt-Väisälä frequency (N^2) derived from perturbed temperatures. A high-pass band filter with a one-hour interval cut-off frequency is applied to the perturbed temperature

330   (T$_p$) data before deriving the waves' potential energy. This process covers the period from 2005 to

331   2020 at selected heights of 90, 85, 75, and 70 km (see Figure 10 a-d). The high-pass band filter

332   eliminates the influence of long-period oscillations, such as tidal or planetary waves, on the

333   inversion, isolating the gravity waves (Gw). The effects of the high-pass band filter are visible in

334   Figure 10 (a-d), showing the upper mesosphere at 90 and 85 km and the lower mesosphere at 75

335   and 70 km. The filter reduces the amplitude of the perturbed temperature in the upper mesosphere

336   (90 and 85 km) from approximately ~(-20 to 20 K) to ~(-10 to 10 K). It also reduces the amplitude

337   in the lower mesosphere from ~(-20 to 20 K) to ~(-8 to 8 K) by eliminating higher amplitudes.
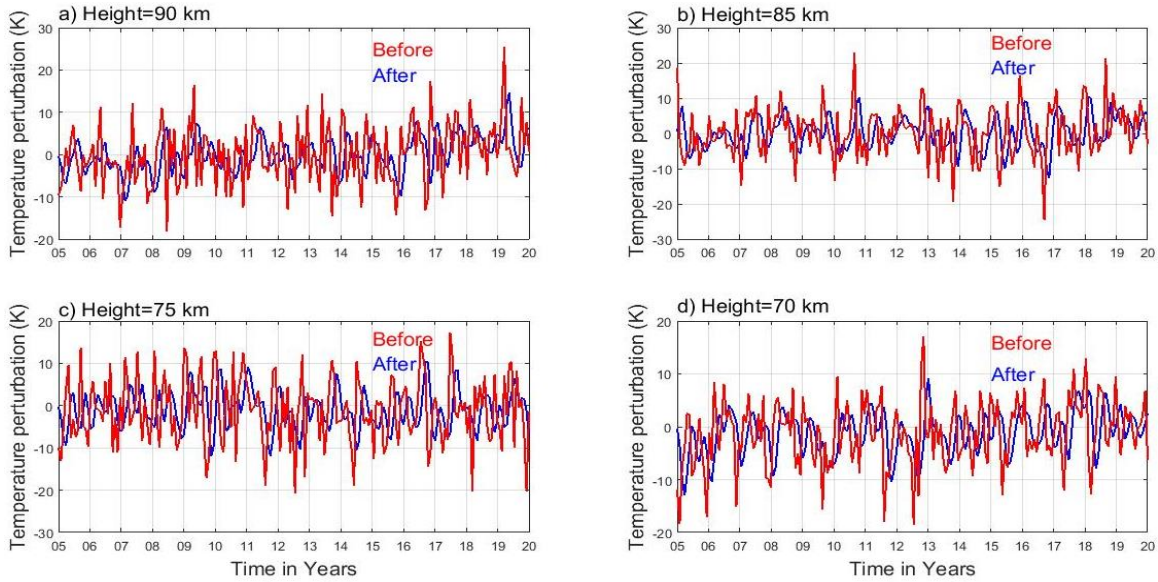
338

339   **Figure** 10. Perturbed temperature profiles before (red color) and after (blue color) applying the

340   low-pass band filter for the upper (85 and 90 km) and lower (70 and 75 km) regions.

341   Potential energy (Ep) is constructed using the time series filtered perturbed temperature (Tp') at

342   selected heights of 90, 85, 75, and 70 km. This approach is based on the fact that gravity wave

343   activity is represented by potential energy, as described by numerous authors (Tsuda et al., 2000;

344   Wang and Geller, 2003; Liu et al., 2014; Thurairajah et al., 2014). Figure 11 (a-d) demonstrates

345   the spatiotemporal variability of gravity wave potential energy, showing the upper mesosphere

346   region at 90 and 85 km and the lower mesosphere region at 75 and 70 km.
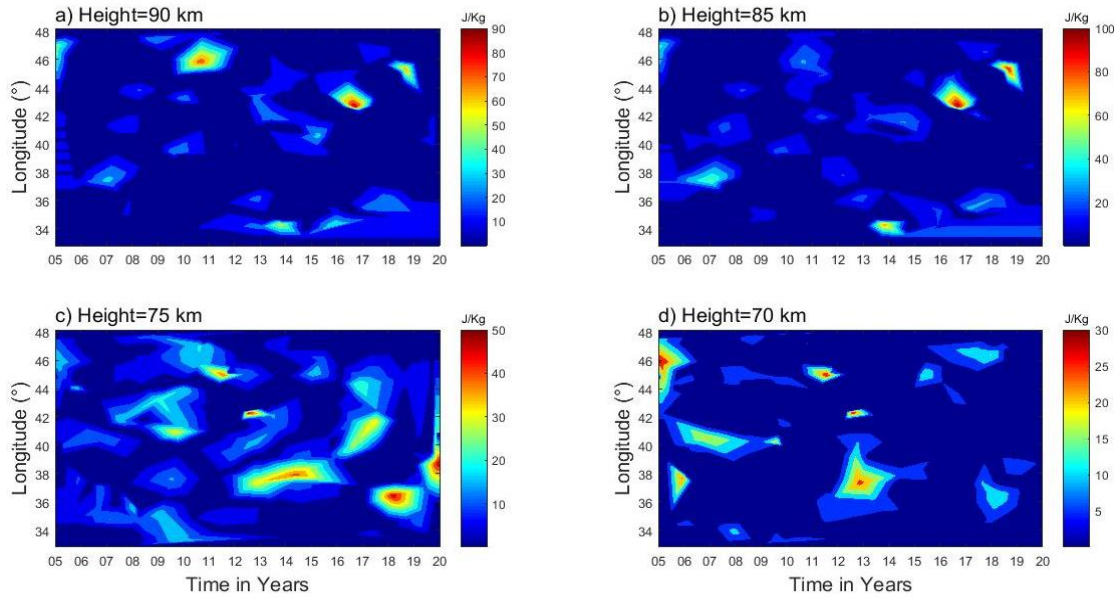
Figure 11. Gravity wave potential energy for the upper (85 and 90 km) and lower (70 and 75 km) mesosphere regions.

Figure 11(a) shows maximum gravity wave potential energies, ranging from ~70 to 90 J/kg, over the longitudinal regions of 45-47° E, 43° E, and 44° E during 2011, 2017, and 2019 for upper mesosphere inversions at 90 km. In contrast, potential energies around ~10 to 60 J/kg are present across the entire longitudinal region from 33-48° E. Figure 11(b) shows maximum potential energies of ~70 to 100 J/kg over the longitudinal regions of 34°, 44°, and 46° E during 2014, 2016, and 2018 at 85 km. Minimum potential energies between 20 and 70 J/kg appear over the longitude regions from 33-48° E. Figures 11(c) and 11(d) depict the gravity wave potential energy in the lower MLT regions at 75 and 70 km, respectively. At 75 km, Figure 11(c) shows a relative maximum potential energy of 40-50 J/kg over the longitudinal regions of 46°, 42°, 40°, 37°, 36°, and 38° E during 2011, 2012, 2017, 2013–2015, 2018, and 2020. Similarly, Figure 11(d) illustrates gravity wave potential energy ranging from 2-30 J/kg at 70 km across the longitudinal region of 33-48° E. Maximum potential energy of 25-30 J/kg is observed in certain longitudinal regions over time.

Gravity wave breaking in the upper atmosphere usually leads to more turbulence and mixing. As gravity waves rise and break, they transform their potential and kinetic energy into turbulent energy. This process increases vertical mixing and transports momentum. This energy transfer can change thermal patterns and affect the overall dynamics of the upper atmosphere. Interestingly, the dissipation of gravity waves can lead to localized warming or the formation of mesospheric

368   inversion layers (MILs). This is especially important in the upper mesosphere and lower

369   thermosphere, where wave breaking can significantly impact the thermal structure. Gravity wave

370   propagation and dissipation are major forces in the MLT region (Lindzen, 1981; Holton, 1983),

371   influencing middle and upper atmospheric inversion. In a nutshell, gravity wave breaking and the

372   dissipation of energy and momentum are key players in both the upper and lower atmospheres,

373   affecting turbulence, circulation patterns, temperature, density, and weather systems.

374   Gravity waves come in different sizes, with smaller waves being the main derivers of instability

375   and turbulence in the MLT (mesosphere and lower thermosphere) region (Liu and Meriwether,

376   2004; Szewczyk et al., 2013). Hauchecorne et al. (1987) proposed a model where a series of

377   breaking gravity waves leads to the formation of MILs through the gradual accumulation of heat,

378   which contributes to instability. Understanding mesospheric inversion layer (MIL) phenomena is

379   crucial for understanding MLT atmospheric dynamics, especially when it comes to stability and

380   energy transfer. To investigate the role of gravity waves in MLT instability, the Brunt-Väisälä

381   frequency was used. Contour plots in Figure 12 (a-d) show the spatiotemporal variability of the

382   Brunt-Väisälä frequency, with Figures 12(a and b) representing the upper mesosphere (90 and 85

383   km) and Figures 12(c and d) representing the lower mesosphere (75 and 70 km). The Brunt-Väisälä

384   frequency (N^2) shows that the upper MLT region is more unstable (~0.027 at 90 km and ~0.029 at

385   85 km) than the lower mesosphere (~0.033 at 75 km and ~0.035 at 70 km).
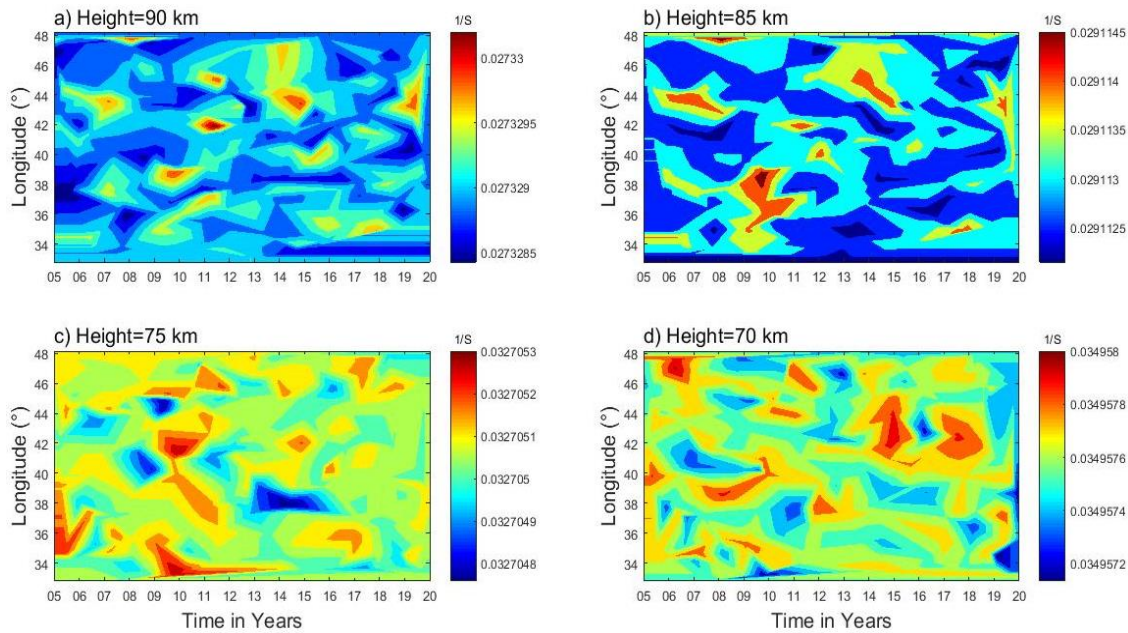
386

387   Figure 12. Brunt-Vaisala frequency (N^2) profiles for the upper (85 and 90 km) and lower (70 and

388   75 km) mesosphere regions.

4. Summary

In this article, 16 years of SABER MLT temperature profiles are utilized to investigate the MIL phenomenon and its causative mechanism through gravity wave potential energy (P_E) and instability criteria of Brunt-Väisälä frequency (N^2) over low latitude bands. The following conclusions are drawn from the observations in this article:

- ✓ The upper mesosphere inversion frequency occurs more often than the lower mesosphere inversion.
- ✓ Analysis of the MIL characteristic features reveals the most probable values for the upper inversion: amplitude of 38 k, thickness of 5.5 km, and base height of 78 km. The lower inversion has an amplitude of 25 K, a thickness of 3.8 km, and a base height of 73 km.
- ✓ The upper mesosphere region has higher gravity wave potential energy compared to the lower mesosphere region.
- ✓ The high potential energy in the upper mesosphere region is likely due to the deposition of energy and momentum by gravity wave breaking. This could influence the dynamics of the inversion phenomenon.
- ✓ The Brunt-Väisälä frequency (N^2) indicates that the upper mesosphere region is less stable than the lower mesosphere region. This lower stability contributes to the high potential energy in the upper mesosphere, which leads to larger inversion phenomena.
- ✓ Atmospheric processes vary significantly from region to region, with altitude, and over time.

D*ata availability.* The SABER data are freely available via the link at http://saber.gats-inc.com/index.php.

Author contribution. Chalachew Lingerew: data curation, investigation, software, visualization, writing the original draft, and writing review. U. Jaya Prakash Raju; supervision, and editing.

Competing interest. The authors declare that they have no conflict of interest relevant to this study.

Acknowledgments. The Authors would like to express their gratitude to the National Aeronautics and Space Administration (NASA) for providing the SABER data downloaded from the website: http://saber.gats-inc.com/index.php.

References

Begue, N., Mbatha, N., Bencherif, H., Loua, R. T., Siva Kumar, V., & Leblanc, T.: Statistical analysis of the mesospheric inversion layers over two symmetrical tropical sites: Reunion (20.8° S, 55.5° E) and Mauna Loa (19.5° N, 155.6° W). *In Annales Geophysicae,* 35, 1177-1194, 2017.

Bizuneh, C.L., Prakash, R., and Nigussie, M.: Long-term temperature and ozone response to natural drivers in the mesospheric region using 16 years (2005–2020) of TIMED/SABER observation data at $5\text{-}15^0$N. Advances in Space Research, 70, 2095–2111, https://doi.org/10.1016/j.asr.2022. 06.051, 2022.

Collins, R. L., Lehmacher, G. A., Larsen, M. F., and Mizutani, K.: Estimates of vertical eddy diffusivity in the upper mesosphere in the presence of a mesospheric inversion layer, Ann. Geophys., 29(11), 2019–2029, http://doi:10.5194/angeo-29-2019-2011, 2011.

Cutler, L. J., Collins, R. L., Mizutani, K., and Itabe, T.: Rayleigh lidar observations of mesospheric inversion layers at Poker Flat, Alaska (65^0 N, 14^0 W), Geophys. Res. Lett., 28, 1467–1470, https://doi.org/10.1029/2000GL012535, 2001.

Dou, X., Li, T., Xu, J., Liu, H. L., Xue, X., Wang, S., Leblanc, T., McDermid, I. S., Hauchecorne, A., Keckhut, P., Bencherif, H., Heinselman, C., Steinbrecht, W., Mlynczak, M. G., and Russell III, J. M.: Seasonal oscillations of middle atmosphere temperature observed by Rayleigh lidars and their comparisons with TIMED/SABER observations, J. Geophys. Res., 114, D20103, https://doi.org/10.1029/2008JD011654, 2009.

Duck, T. J., Sipler, D. P., and Salah, J. E.: Rayleigh lidar observations of a mesospheric inversion layer during night and day, Geophys. Res. Lett., 28, 3597–3600, 2001.

Duck, T. J. and Greene, M. D.: High Arctic observations of mesospheric inversion layers, Geophys. Res. Lett., 31, L02105, https://doi.org/10.1029/2003GL018481, 2004.

Eckermann, S.D., Hirota, I., and Hocking, W. K.: Gravity wave and equatorial wave morphology of the stratosphere derived from long-term rocket soundings. Q. J. R. Meteorol. Soc., 121, 149 186, http://doi.org/10.1002/qj.49712152108, 1994.

Emanuel, K.A.: Atmospheric Convection, Oxford University Press, New York, 580pp, 1994.

Fechine, J., Wrasse, C. M., Takahashi, H., Mlynczak, M. G., and Russell, J. M.: Lower-mesospheric inversion layers over Brazilian equatorial region using TIMED/SABER temperature profiles, Adv. Space Res., 41, 1447–1453, https://doi.org/10.1016/j.asr.2007. 04.070, 2008.

Fritts, D. C., Wang, L., Laughman, B., Lund, T. S., & Collins, R. L.: Gravity wave dynamics in a mesospheric inversion layer: 2. Instabilities, turbulence, fluxes, and mixing. Journal of

Geophysical Research: Atmospheres, 123, 649–670, https://doi.org/10.1002/2017JD027442, 2018.

France, J. A., Harvey, V. L., Randall, C. E., Collins, R. L., Smith, A. K., Peck, E. D., and Fang, X.: A climatology of planetary wave-driven mesospheric inversion layers in the extratropical winter, J. Geophys. Res.-Atmos., 120, 399–413, https://doi.org/10.1002/2014JD022244, 2015.

Fritts, D. C., and Alexander, M. J.: Gravity wave dynamics and effects in the middle atmosphere, Rev. Geophys., 41, 1003, https://doi.org/10.1029/2001RG000106, 2003.

Fritts, D. C., Laughman, B., Wang, L., Lund, T. S., & Collins, R. L.: Gravity wave dynamics in a mesospheric inversion layer: 1. Reflection, trapping, and instability dynamics. Journal of Geophysical Research: Atmospheres, 123, 626-648, https://doi.org/10.1002/2017JD027440, 2018.

Gan, Q., Zhang, S. D., and Yi, F.: TIMED/SABER observations of lower mesospheric inversion layers at low and middle latitudes, J. Geophys. Res., 117, D07109, https://doi:0.1029/2012JD 017455, 2012.

Garcia-Comas, M., Lopez-Puertas, M., Marshall, B. T., Winter Steiner, P. P., Funke, B., Bermejo-Pantaleon, D., Mertens, C. J., Remsberg, E. E., Gordley, L. L., Mlynczak, M. G., and Russell III, J. M.: Errors in Sounding of the Atmosphere using Broadband Emission Radiometry (SABER) kinetic temperature caused by non-local-thermodynamic-equilibrium model parameters, J. Geophys. Res., 113, D24106, doi: 10.1029/2008JD010105, 2008.

Hirota, I.: Climatology of gravity waves in the middle atmosphere. J. Atmos. Terr. Phys., 46, 767–773, http://doi.org/10.2151/jmsj1965.63.6-1055, 1984.

Hamilton, K.: Climatological Statistics of Stratospheric Inertia-Gravity Waves Deduced from Historical Rocket-sonde Wind and Temperature Data. J. Geophys. Res., 96, 20831–20839, http://doi.org/10.1029/91JD02188, 1991.

Hauchecorne, A., Chanin, M. L., & Wilson, R.: Mesospheric temperature inversion and gravity wave breaking. *Geophysical Research Letters*, 14(9), 933-936, https://doi.org/10.1029/ GL014i009p00933, 1987.

Holton, J. R., Curry, J. A., and Pyle, J. A.: *Encyclopedia of atmospheric sciences*, volume 1. Academic Press, 2003.

Holton, J. R.: The influence of gravity wave breaking on the general circulation of the middle atmosphere, J. Atmos. Sci., 40, 2497–2507, 1983.

Holton, J. R. and Hakim, G. J.: *An introduction to dynamic meteorology*. Academic Press, 2013.

Irving, B. K., Collins, R. L., Lieberman, R. S., Thurairajah, B., and Mizutani, K.: Mesospheric Inversion Layers at Chatanika, Alaska (65°N, 147°W): Rayleigh lidar observations and analysis, J. Geophys. Res. Atmos., 119, 11,235–249, http://doi:10.1002/2014JD021838, 2014.

John, S.R., Kumar, K. K.: TIMED/SABER observations of global gravity wave climatology and their interannual variability from stratosphere to mesosphere lower thermosphere. Clim. Dyn., 39, 1489–1505, http://doi.org/10.1007/s00382-012-1329-9, 2012.

Leblanc, T., McDermid, I. S., Hauchecorne, A., and Keck hut, P.: Evaluation of optimization of lidar temperature analysis algorithms using simulated data, J. Geophys. Res., 103, 6177–6187, 1998.

Leblanc, T., and Hauchecorne, A.: Recent observations of mesospheric temperature inversions, J. Geophys. Res., 102, 19471–19482, https://doi.org/10.1029/97JD01445, 1997.

Lindzen, R. S.: Turbulence and stress due to gravity waves and tidal breakdown, J. Geophys. Res., 86, 9707–9714, https://doi:10.1029/JC086iC10p09707, 1981.

Lingerew, C., Jaya Prakash Raju, U., & Guimarães Santos, C. A.: NN-MLT model prediction for low-latitude region based on artificial neural network and long-term SABER observations. *Earth and Space Science*, *10*, e2023EA002930, https://doi.org/10.1029/2023 EA002930, 2023.

Liu, S-D., and S-S. Liu: *Atmosphere Dynamics*, Peking University Press, Beijing, 2011.

Liu, H. L., Hagan, M. E., & Roble, R. G.: Local mean state changes due to gravity wave breaking modulated by the diurnal tide. *Journal of Geophysical Research*, 105(D10), 12381-12396, (2000).

Liu, H. L., & Hagan, M. E.: Local heating/cooling of Atmospheres. 96(D8), 15297-15309, (1998).

Mlynczak, M. G., Marshall, B. T., Martin-Torres, F. J., Russell III, J. M., Thompson, R. E., Remsberg, E. E., and Gordley, L. L.: Sounding of the Atmosphere using Broadband Emission Radiometry observations of daytime mesospheric O_2 (1Δ) 1.27 μm emission and derivation of ozone, atomic oxygen, and solar and chemical energy deposition rates, 2007.

Meriwether, J. W., and Gerrard, A. J.: Mesosphere inversion layers and stratosphere temperature enhancements, Rev. Geophys., 42, RG3003, http//doi:10.1029/2003RG000133, 2004.

Meriwether, J. W., and Gardner, C. S.: A review of the mesosphere inversion layer phenomenon, J. Geophys. Res., 105, 12 405–12 416, 2000.

Nath, O., & Sridharan, S.: Long-term variabilities and tendencies in zonal mean TIMED–SABER ozone and temperature in the middle atmosphere at 10–15°N. Journal of Atmospheric and Solar-Terrestrial Physics, 120, 1–8, https://doi:10.1016/j.jastp.2014.08.010, 2014.

Ramesh, K., Sridharan, S.: Large mesospheric inversion layer due to breaking of small scale gravity waves: Evidence from Rayleigh lidar observations over Gadanki (13.51^0 N, 79.21^0 E). J. Atmos. Sol. Terr. Phys. 89, 90–97, http://doi.org/10.1016/j.jastp.2012.08.011, 2012.

Ramesh, K., Sridharan, S. and Vijaya Bhaskara, S.: Causative mechanisms for the occurrence of a triple-layered mesospheric inversion event over low latitudes, J. Geophys. Res. Space Physics, 119, 3930–3943, http://doi:10.1002/2013JA019750, 2014.

Ramesh, K., Sridharan, S., Raghunath, K., and Rao, S. V. B.: A chemical perspective of day and night tropical (10°N–15°N) mesospheric inversion layers, J. Geophys. Res. Space Physics, 122, http://doi:10.1002/2016JA023721, 2017.

Ramesh, K., Sridharan, S., Vijaya Bhaskara Rao, S., Raghunath, K., Bhavani Kumar, K.: Rayleigh lidar observations of mesospheric inversion layers over Gadanki (13.5^{0}N, 79.2^0 E) and their relation with gravity wave activities. Indian Journal of Radio and Space Science, 43, 83-90, 2013.

Remsberg, E., Lingenfelser, V., Harvey, V., Grose, W., Russell III, J., Mlynczak, M., Gordley, L., and Marshall, B. T.: The verification of the quality of SABER temperature, geopotential height, and wind fields by comparison with Met Office assimilated analyses, J. Geophys. Res., 108(D19), 4628, https://doi:10.1029/2003JD003720, 2003.

Rezac, L., Kutepov, A., Russell, J.M., Feofilov, A.G., Yue, J., and Goldberg, R.A.: Simultaneous retrieval of T (p) and CO2 VMR from two-channel non-LTE limb radiances and application to daytime SABER/ TIMED measurements. J. Atmos. Sol. Terr. Phys 130–131, 23–42. https://doi.org/10.1016/j.jastp.2015.05.004, 2015.

Russell, J.M., Mlynczak, M.G., Gordley, L.L., Tansock, J., Esplin, R.: An overview of the SABER experiment and preliminary calibration results. In Proceedings of the SPIE, 44th Annual Meeting, Denver, CO, USA, 3756, 277–288, 1999.

Schmidlin, F. J.: Temperature inversions near 75 km. *Geophysical Research Letters*, 3(3), 173-176, (1976).

Sica, R. J., Argall, P. S., Shepherd, T. G., and Koshyk, J. N.: Model-measurement comparison of mesospheric temperature inversions, and a simple theory for their occurrence, Geophys. Res. Lett., 34, L23806, https://doi:10.1029/2007GL030627, 2007.

Sivakandan, M., Kapasi, D., and Taori, A.: The occurrence altitudes of middle atmospheric temperature inversions and mesopause over low-latitude Indian sector, Ann. Geophys., 32, 967–974, https://doi.org/10.5194/angeo-32-967-2014, 2014.

Siva Kumar, V., Bhavani Kumar, Y., Raghunath, K., Rao, P. B., Krishnaiah, M., Mizutani, K., Aoki, T., Yasui, M., and Itabe, T.: Lidar measurements of mesospheric temperature inversion at a low latitude, Ann. Geophys., 19, 1039–1044, https://doi.org/10.5194/angeo-19-1039-2001, 2001.

Sridharan, S., Sathishkumar, S., and Gurubaran, S.: Influence of gravity waves and tides on mesospheric temperature inversion layers: simultaneous Rayleigh lidar and MF radar observations, Ann. Geophys., 26, 3731–3739, 2008.

Singh, R. P., & Pallamraju, D.: Mesospheric temperature inversions observed in OH and O2 rotational temperatures from Mount Abu (24.6°N, 72.8°E), India. Journal of Geophysical Research: Space Physics, 123, 8823–8834, https://doi.org/10.1029/2018JA025703, 2018.

Smith, A.: Global Dynamics of the MLT, Surv. Geophys, 33, 1177–1230, https://doi.org/10.1007/s10712-012-9196-9, 2012.

Szewczyk, A., Strelnikov, B., Rapp, M., Strelnikova, I., Baumgarten, G., Kaifler, N., Dunker, T., and Hoppe, U. P.: Simultaneous observations of a Mesospheric Inversion Layer and turbulence during the ECOMA-2010 rocket campaign, Ann. Geophys., 31, 775–785, http://doi:10.5194/angeo-31-775-2013, 2013.

Vadas, S. L., and Fritts, D. C.: Thermosphere responses to gravity waves: Influences of increasing viscosity and thermal diffusivity, J. Geophys. Res., VOL. 110, D15103, doi: 10.1029/2004JD005574, 2005.

Wang, L., Geller, M.A., Alexander, M.J.: Spatial and Temporal Variations of Gravity Wave Parameters. Part I: Intrinsic Frequency, Wavelength, and Vertical Propagation Direction. J. Atmos. Sci., 62, 125–142, http://doi.org/10.1029/2010JD013860, 2005.

Wang, L., and Alexander, M.J.: Global estimates of gravity wave parameters from GPS radio occultation temperature data. J. Geophys.Res. 115, D21122, http://doi.org/10.1029/2010JD013860, 2010.

Walterscheid, R. L., and Hickey, M. P.: Gravity wave ducting in the upper mesosphere and lower thermosphere duct system, J. Geophys. Res., 114, D19109, http://doi:10.1029/2008JD 011269, 2009.

Yuan, T., Pautet, P. D., Zhao, Y., Cai, X., Criddle, N. R., Taylor, M. J., and Pendleton, W. R.: Coordinated investigation of mid-latitude upper mesospheric temperature inversion layers and the associated gravity wave forcing in Logan, Utah, J. Geophys. Res. Atmos., 119, 3756–3769, http://doi:10.1002/2013JD020586, 2014.